Photoluminescence Quenching and Charge Transfer in Artificial Heterostacks of Monolayer Transition Metal Dichalcogenides and Few-Layer Black Phosphorus

Jiangtan Yuan,[§,†] Sina Najmaei,[§,†] Zhuhua Zhang,[§,⊥] Jing Zhang,[§] Sidong Lei,[§] Pulickel M. Ajayan,[§] Boris I. Yakobson,[§] and Jun Lou[§,*]

[§]Department of Materials Science and NanoEngineering, Rice University, Houston, Texas 77005, United States and [⊥]State Key Laboratory of Mechanics and Control of Mechanical Structures and Key Laboratory of Intelligent Nano Materials and Devices of MoE, Nanjing University of Aeronautics and Astronautics, Nanjing 210016, China. [†]These authors (J.Y. and S.N.) contributed equally to the work.

ABSTRACT Transition metal dichalcogenides monolayers and black phosphorus thin crystals are emerging two-dimensional materials that demonstrated extraordinary optoelectronic properties. Exotic properties and physics may arise when atomic layers of different materials are stacked together to form van der Waals solids. Understanding the important interlayer couplings in such heterostructures could provide avenues for control and creation of characteristics in these artificial stacks. Here we systematically investigate the optical and optoelectronic properties of artificial stacks of molybdenum disulfide, tungsten disulfide, and black phosphorus atomic layers. An anomalous photoluminescence quenching was observed in tungsten disulfide—molybdenum disulfide stacks. This was attributed to a direct to indirect band gap transition of tungsten disulfide in such stacks while molybdenum disulfide maintains its monolayer properties by first-principles calculations. On the other hand, due to the strong build-in electric fields in tungsten disulfide—black phosphorus or molybdenum disulfide—black phosphorus stacks, the excitons can be efficiently splitted despite both the component layers having a direct band gap in these stacks. We further examine optoelectronic properties of tungsten disulfide—molybdenum disulfide artificial stacks and demonstrate their great potentials in future optoelectronic applications.

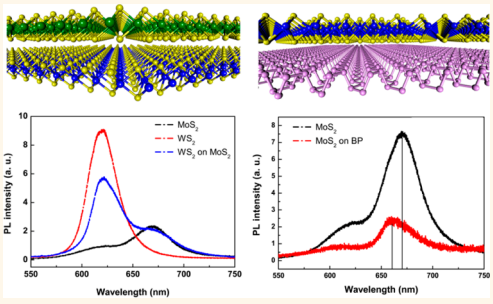

KEYWORDS: transition metal dichalcogenides · black phosphorus · photoluminescence · charge transfer · optoelectronics

The exciting physics of two-dimensional (2D) materials have been extensively studied in graphene.[1−6] However, the absence of a band gap in the electronic structure of graphene imposes limitations in many of its possible applications.[5,7] Inspired by their implications, a growing interest has recently been focused on other 2D materials beyond graphene.[8−15] Among these materials, 2D transitional metal dichalcogenides (TMDs) made of transition metals in groups IV, V, VI, and VII, and chalcogens such as S, Se, or Te are particularly interesting owing to their richness in material compositions and electronic structures.[10,16] Their monolayer structures typically consist of a plane of metal atoms sandwiched by two planes of chalcogens.[17,18] MoS_2 and WS_2 monolayers are two most widely studied 2D TMDs with unique electrical and optical properties. Similar to graphene, many approaches such as mechanical exfoliation,[8,11,19] chemical exfoliation[17,20] and chemical vapor deposition (CVD)[21−23] have been explored for their preparations.

When exfoliated from the bulk, monolayer MoS_2 will transform from an indirect band gap semiconductor to a direct band gap semiconductor. Accordingly, the band gap will change from ∼1.2 to ∼1.9 eV.[24] WS_2 shows similar trends as predicted by calculations[25,26] and confirmed by experiments.[27] However, in order to meet the demand of realistic device applications, it is very important to establish strategies to modulate physical properties of these

* Address correspondence to jlou@rice.edu.

Received for review October 11, 2014 and accepted January 8, 2015.

Published online January 08, 2015
10.1021/nn505809d

emerging 2D semiconductors.[28] One very promising approach to afford such property modulation is by creating artificial stacks of dissimilar 2D TMDs,[26] which has recently been demonstrated in transistor and solar cell devices. The development of tunneling field effect transistor with high on/off ratios of $\sim 10^6$,[29] high photocurrent generation with the external quantum efficiency larger than 30%, and large absorption properties in these heterostructured stacks makes good examples of this approach.[30,31] The similar structural properties of monolayer MoS_2, WS_2 and other 2D TMDs combined with their unique band structure differences suggest fascinating possibilities as they are brought together,[32−35] and deserve further examinations.

Meanwhile, black phosphorus (BP) has recently attracted huge attention as it is the bulk phase of phosphorene, a new member of the 2D materials family. Few-layer BP has shown well-behaved p-type characteristics with a high carrier mobility of $\sim$1000 $cm^2/V \cdot s$, in contrast to n-type MoS_2 and WS_2.[36,37] Therefore, one would expect very different interactions between MoS_2−WS_2 stacks and MoS_2−BP, WS_2−BP stacks. However, the understanding of interlayer coupling behavior between 2D TMDs and BP still remains elusive.

In this work, we systematically investigate the Raman and photoluminescence (PL) properties of artificial TMD bilayer stacks of MoS_2, WS_2, MoS_2−WS_2 heterostructures with varied stacking order, as well as MoS_2−BP, WS_2−BP stacks. We first demonstrate the effectiveness of the preparation method by comparing our results to reports on natural bilayers. Next, we employ our approach to prepare MoS_2−WS_2 and MoS_2−BP, WS_2−BP stacks and characterize their corresponding Raman and PL properties. Our finding shows that while only WS_2 has a significant PL quenching effect in the artificial stacked heterostructures of MoS_2−WS_2, both MoS_2 and WS_2 show dramatic quenching in MoS_2−BP and WS_2−BP heterostacks. Furthermore, both PL peaks of MoS_2 and WS_2 have a blue-shift after forming stacks with BP. We explore possible mechanisms behind these observations using first-principles calculations. Our calculation indicates that the interactions between MoS_2 and WS_2 layers retain the direct band gap at the K point in the MoS_2 layer while an indirect gap formed in the WS_2 layer. This explains the observed weakening of PL peak in WS_2 as indirect band gap requires the participation of phonon in PL process. In MoS_2−BP and WS_2−BP heterostacks, the MoS_2−BP shows a type-II band alignment and WS_2−BP has a type-I band alignment. Both component layers have a direct band gap, but the build-in electric fields in these stacks are strong enough to split the excitons, leading to a significant reduction in their recombination, and this explains the PL peak of MoS_2 remaining impaired in such direct-gap system. Also, the band gap of MX_2 layer in these heterostructures is slightly reduced by about 10 meV compared to the value in freestanding case, which is in excellent agreement with our blue-shift measurements of the coresponding PL peaks. We finally characterize the photodetector properties of typical MoS_2−WS_2 stacks suggesting potential applications in future optoelectronics.

RESULTS AND DISCUSSION

To prepare artificial stacks, we utilized a liquid transfer technique described in Figure 1. Two steps of transfer were applied with poly(methyl methacrylate) (PMMA) as medium and NaOH as etchant (Supporting Information). By using this liquid transfer technique, we are able to prepare MoS_2 bilayers, WS_2 bilayers, WS_2−MoS_2 (with alternate sequences), MoS_2−BP (top/bottom), and WS_2−BP (top/bottom) heterostacks. Figure 1 shows a schematic illustration of the transfer process and a typical optical image of these heterostacks with WS_2−MoS_2 (top/bottom) configuration at the end of step 2. The effectiveness of the transferring technique is confirmed by careful Raman and PL evaluations of artificial stacks of bilayer MoS_2 and WS_2 as compared to their natural bilayer counterparts (see Supporting Information).

After successful preparation of different artificial stacks, we next probe the Raman and PL properties of WS_2 and MoS_2 heterostructures. We prepare these stacks with alternative top-bottom sequences in order to take into account of the environmental and dielectric effects. It is known that the dielectric environment can have significant effect on the band gap properties of these atomic layers.[38] Therefore, to have a comprehensive investigation of the stacking order role, we alternate the stacking sequence with the understanding that the monolayer on top will experience different dielectric environments as in the reversed stacking order. Figure 2a shows the Raman spectra of MoS_2 only area (black dotted line), WS_2 only area (red dotted line), and the stacked area (blue dotted line) for the WS_2−MoS_2 (top/bottom) bilayer heterostructures. It can be clearly seen that the overlapped area has both the peaks from MoS_2 and WS_2, indicating the existence of both MoS_2 and WS_2. The Raman peak positions show little change as compared to pristine samples of each type. This indicates that the van der Waals interactions, stacking-induced structural changes, and long-range Coulombic interactions are not strong enough in these stacks to induce shifts in the Raman modes of these bilayers. However, the normalized PL characteristics of the stacked area in Figure 2c show a distinctly different behavior. In the non-overlapped area, the PL of WS_2 has a much higher intensity than that of MoS_2. The normalized intensity of WS_2 is $\sim$9.1 and that of MoS_2 is $\sim$2.3. But in the stacked area, the intensity of WS_2 quenches to $\sim$5.6, a decrease of $\sim$38.5%, while the PL intensity of MoS_2 has a lesser change.

To confirm this phenomenon is not induced by the dielectric environment, we next consider the alternative stacking sequence and its role in the PL

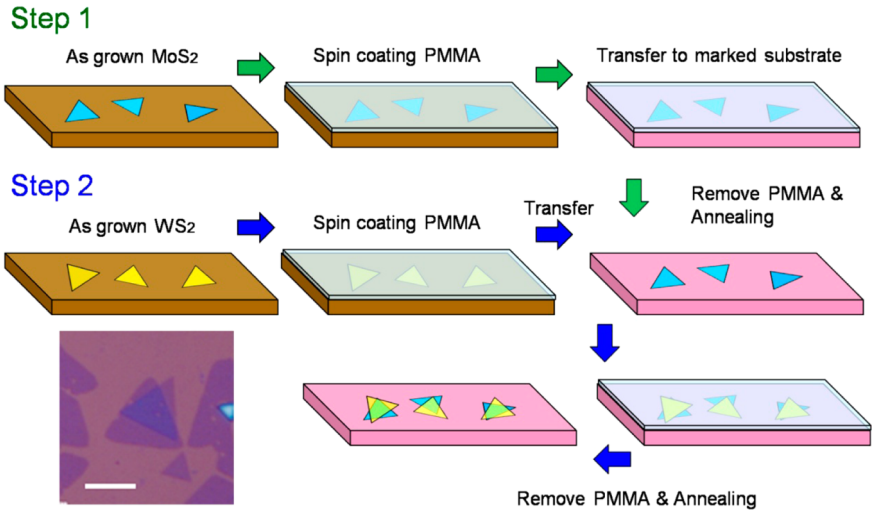

Figure 1. In step 1, PMMA is coated on MoS_2 as grown on SiO_2/Si substrate (brown). After etching SiO_2 substrate with NaOH, the PMMA film with MoS_2 samples was transferred to marked SiO_2/Si substrate (pink). PMMA is then removed by DMF and rinsed thoroughly in DI water. To remove the remaining residues, sample is annealed at 200 °C using a mixture of H_2/N_2 (20% H_2, 80% N_2) at pressure of 0.1 Torr for 1 h. In step 2, using the same procedure, we transfer WS_2 to the same marked Si substrate. After removing PMMA, a second annealing using the same conditions is applied to make sure the two layers contact well with each other. Inset: typical optical picture of heterostacks; the scale bar is 5 μm.

quenching observed in heterobilayer of MoS_2 and WS_2. The Raman spectra acquired from MoS_2–WS_2 (top/bottom) stacks in Figure 2b show clear peaks for MoS_2 and WS_2. The signature difference between the spectrum and Figure 2a is the change in the relative intensity of the two species. As expected in this configuration, the intensity of MoS_2 peaks is stronger and WS_2 signal is weaker. However, no change in the peak positions is observable, similar to the earlier stacking configuration discussed before. For the PL spectra in the stacking area (Figure 2d), the intensity of WS_2 decreases even more significantly, from ~10.8 to ~4.4, a decrease of ~59.3%. This further confirms the observed WS_2 PL quenching behavior in these stacks. Compared to the stacks made of the same materials, the heterostacks are made of two different materials with mismatched band positions; WS_2 has a lower work function of ~4.6 eV compared to that of MoS_2 of ~5.1 eV.[31,39] The band mismatch could potentially induce interactions between WS_2 and MoS_2 layers resulting in the observed anomalous PL behaviors.

To gain further insight into the PL intensity changes in the heterobilayers of MoS_2 and WS_2, we perform first-principles electronic structure calculations based on density-functional theory as implemented in VASP code (see Method section for details).[40−42] Figure 2e presents the band structure of MoS_2–WS_2 heterobilayer, which overall displays a distinct indirect band gap. However, the electronic feature differs in the two component layers: the MoS_2 layer retains a direct band gap at the K point ,while the WS_2 layer has formed an indirect gap around the Fermi level, with the valence band maximum (VBM) at Γ point and conduction band minmum (CBM) at K point. As the indirect band gap requires the aid of phonon for PL, the conresponding peak is significantly weakened (now the PL peak of WS_2 layer should be largely due to its direct band gap at K point that is only 0.11 eV wider than the indirect gap), whereas the nearly direct band gap in the MoS_2 layer tends to maintain the corresponding PL peak (the formation of trions also contributes to the unchanged PL as discussed later), in good agreement with our experimental observations. Given that VBM at the Γ point contains a fraction of S $3p_z$ states from both layers, the robust PL peak of the MoS_2 layer suggests that the key photo excitation is through the states at the K point, where localized d orbitals enable strong dipole transitions. The layer-dependent electronic feature is in contrast with homogeneous MoS_2 or WS_2 bilayer where both show an indirect band gap and thus significantly weakened PL peaks. The distinct PL features of the two component layers in the heterobilayers of MoS_2 and WS_2 are also attributed to the built-in electric field between the two layers. The electrostatic potential energy profile shows a potential energy difference of 1.3 eV between the W and Mo layers. Indeed, it seems that the bands belonging to the WS_2 layer shift upward with respect to those belonging to the MoS_2 layer, resulting in a type II band alignment (see inset in Figure 2e). The photoexited quasi-particles in the heterostructure may thus be splitted in different layers, further impairing the PL intensity of the system. However, this effect should be the secondary mechanism as the band offset across the heterostructure is only 0.3 eV, less than the exciton binding energy, ~0.8 eV,[43] typical for MX_2 layers. This is also confirmed by calculations using Heyd-Scuseria-Emzerhof (HSE) function. In the HSE band structures of the MoS_2–WS_2

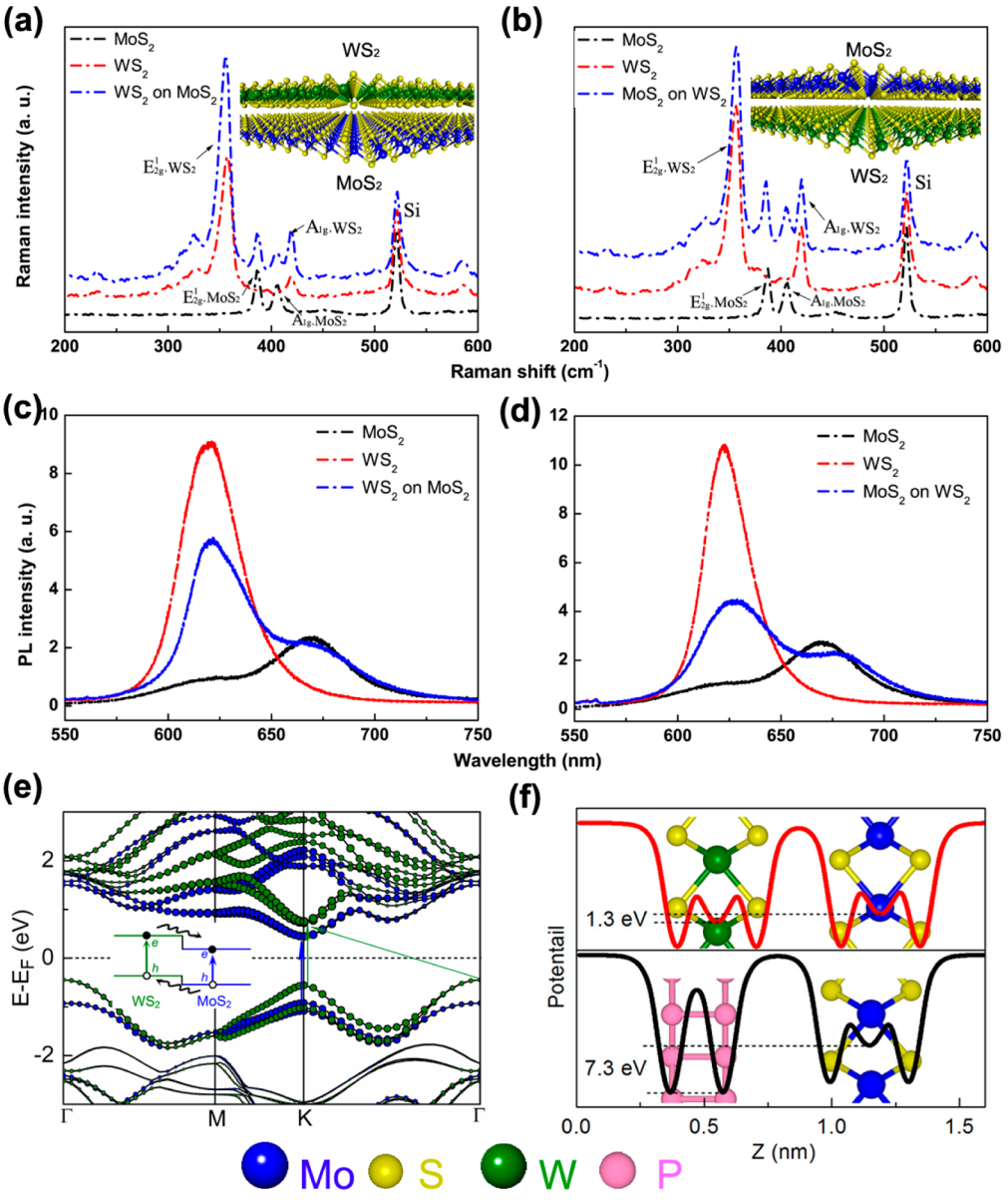

Figure 2. (a) Raman spectra of only MoS_2 (black dotted line), only WS_2 (red dotted line), and the stacked area (blue dotted line) for WS_2−MoS_2 (top/bottom) samples. (b) Raman spectra of only MoS_2 (black dotted line), only WS_2 (red dotted line), and the stacked area (blue dotted line) for MoS_2−WS_2 (top/bottom) stacks. (c) PL spectra for the same areas as in (a). The WS_2 PL intensity decreases ~38.5%, while the PL intensity of MoS_2 has much less change. (d) PL spectra for the same areas as in (b). (e) Electronic band structure of the WS_2−MoS_2 bilayer, with spin−orbit coupling considered. The bands projected to W and Mo 3d orbitals are highlighted by green and blue circles. The circle size reflects the weight of the orbital components in the bands. Inset: schematic band alignment and illustrative transfer of photoexcited carriers within the bilayer. (f) Plane averaged electrostatic potential along the normal of the WS_2−MoS_2 and BP−MoS_2 bilayers. The potential differences across the bilayers are provided.

heterostructure, the band offset is increased to 0.45 eV (Supporting Information Figure S4), still much smaller than the exciton binding energy in 2D MX_2. We also consider the effect of crystal orientation by calculating a randomly stacked MoS_2−WS_2 heterostructure with a twist angle of 28° (Supporting Information Figure S5) and find similar band alignment as in Figure 2e, indicating that the analysis is robust against change in crystal orientation.

It is known that negative trions will be formed as a result of charge accumulation in the charge transfer process.[44−46] Indeed, the main peak in both MoS_2 and WS_2 before stacking can be decomposed into the exciton (X) peak and the negative trion (X^-) peak under the assumption that all the peak are Lorentzian (Supporting Information Figure S2a,b), indicating the unintentional n-doping in MoS_2 and WS_2. Upon stacking these two materials together, by fitting the PL spectrum of the stacked region, we find that in MoS_2, the PL spectral weight of the negative trion (X^-) peak increases compared to that of the exciton (X) peak (Supporting Information Figure S2c), suggesting the

electrons are accumulated additionally in MoS_2. Applying the same analysis to WS_2, we find that WS_2 shows the opposite trend. The spectral weight of the negative trion (X^-) peak decreases compared to that of the exciton (X) peak, indicating that the electrons are depleted from WS_2. This can be understood from our calculations. In MoS_2-WS_2 stacks, electrons tend to transfer from WS_2 layer to MoS_2 layer due to the type II band alignment, resulting in electron accumulation and trion formation in MoS_2, while electron depletion and trion removal in WS_2. However, the drastic decrease of both trion peak and exciton peak (Supporting Information Figure S2c) is different from the literature and cannot be explained solely by the removal of trion. This suggests that the electron depletion is probably only one of the contributing factors to the PL quenching in WS_2. Therefore, we consider the direct to indirect transition in WS_2 as a major reason for the PL quench of WS_2 in MoS_2-WS_2 heterostacks, and attribute the charge transfer between these two component layers as a secondary mechanism. Adjusting the built-in electric field by, for example, intergating the MX_2 layer with other 2D materials is possible to increase the band offset and control the electron−hole separation. This not only allows us to engineer the PL behavior in the bilayer but also improve the performance of TMD based photovoltaic devices, as demonstrated below with black phosphorus and MX_2 heterostructures.

Black phosphorus has recently attracted people's attention as it is the bulk phase of phosphorene, a monolayer analogue of graphene. Few-layer BP has shown well-behaved p-type characteristics with a high carrier mobility of ~1000 $cm^2/V\cdot s$, in contrast to the typical n-type characteristics of MoS_2 and WS_2. Moreover, our first-principles calculations show that the potential difference between the monolayer BP and MoS_2 could reach up to 7.3 eV, almost a 3-fold increase from that between MoS_2 and WS_2 monolayers. Thus, the MoS_2-BP and WS_2-BP heterostacks are anticipated to have different behaviors from the MoS_2-WS_2 or WS_2-MoS_2 heterostacks. Following this rationale, we changed one of our stack materials to exfoliated few-layer BP and prepared MoS_2-BP (top/bottom) and WS_2-BP (top/bottom) heterostacks. The Raman spectra of these stacks are shown in Figure 3a,b. Both MoS_2-BP and WS_2-BP samples show the corresponding characteristic Raman peaks in the stacked area, indicating the successful preparation of stacks of TMDs with BP. However, unlike the earlier scenario in heterostacks of MoS_2 and WS_2 where the PL of MoS_2 only has a slight suppression due to its almost direct band gap structure, in MoS_2-BP and WS_2-BP heterostacks the PL spectra of both MoS_2 and WS_2 show a significant quenching effect: a decrease of ~66.1% in MoS_2 and ~50.9% in WS_2 (Figure 3c,d). In addition, the PL peak of MoS_2 shifts from ~670 to ~661 nm, and the peak of WS_2 shifts from ~621 to ~616 nm, respectively.

Again, we examine the band structure of these two heterobilayers, as shown in Figure 3, panels e and 3f, respectively, by first-principles calculations. For simplicity, we use monolayer BP and MX_2 in our model since the MX_2 monolayer mostly interacts with the top BP layer. Additional calculations using bilayer BP show no significant changes in results. The typical thickness of few-laer BP is ~8 nm, and we can observe the similar phenomenon when MX_2 monolayer is stacked on thicker BP around 20 nm. Interestingly, both component layers in the MoS_2-BP heterostack have a direct band gap at the Γ point, thereby ensuring a high photoadsorption efficiency. However, the MoS_2-BP heterostack shows a type-II band alignment, with a large band offset of 0.8 eV comparable to the exciton binding energy. Therefore, the build-in electric field in the MoS_2-BP heterostack can be strong enough to split the excitons, leading to a significant reduction in their recombination. This well explains our experiment that the PL peak of the MoS_2 is still quenched in such direct-gap system. The same analysis holds for the WS_2-BP heterostack, except that it has a type-I band alignment owing to the higher built-in electric field and larger band gap of the WS_2 layer. As such, there should be a strong PL peak for the BP, but the band gap of multilayer BP (~0.3 eV) is too small to observe the peak with our instruments. Analysis of the trion formation in these two heterostacks (Supporting Information) further suggests the electron accumulation induced by charge transfer between the component layers and can be well understood from our calculations. It is worthy to note that the band gap of MX_2 layer in these heterostructures is slightly reduced by about 10 meV compared to the value in freestanding case, in excellent agreement with our measurements of blue-shift in the corresponding PL peaks. This is because the physical thickness of MX_2 is increased in the heterobilayer, and hence, the quantum confinement effect along the vertical direction is weakened.

To acquire more information about the junction characteristics, we perform electrical and photocurrent measurements on one of the MoS_2-WS_2 heterostacks. The measured current−voltage (IV) of a representative device made from these samples is shown in Figure 4a. The inset in Figure 4a is the device geometry used in our measurements. As expected, the IV shows the characteristics of a strong barrier. Due to the anisotropic transport properties of these atomic layers, one anticipates to see a large barrier for transport between layers. We measure the transfer curves for these devices, which also show the large influence of the barrier, reducing the mobility down to 0.017 ($cm^2/(V\,s)$) as compared to 1−20 ($cm^2/(V\,s)$) in case of MoS_2 (Figure 4b). The mobility was estimated using the equation,

$$\mu = [dI_{ds}/dV_{bg}] \times [L/(WC_iV_{ds})] \quad (1)$$

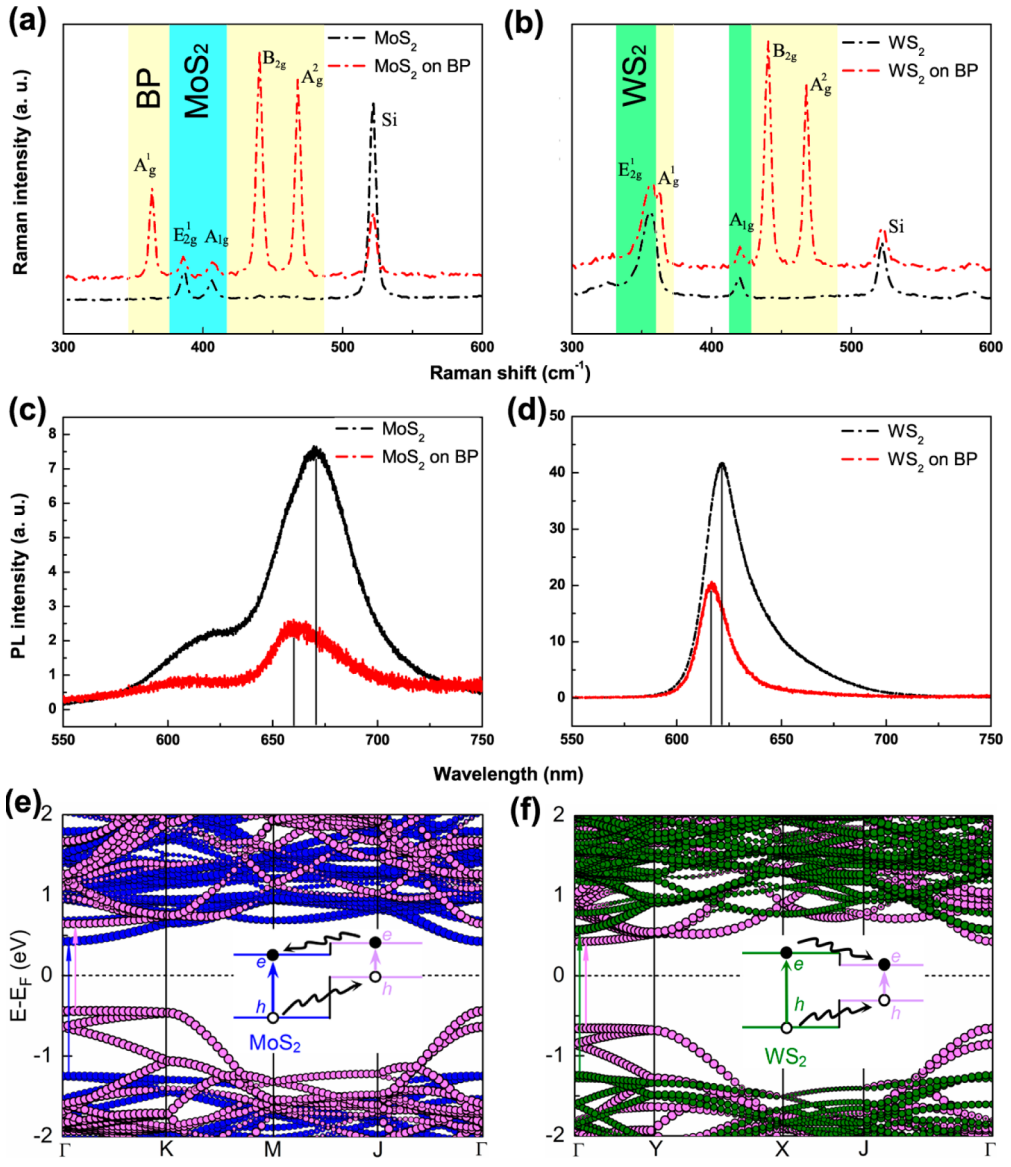

Figure 3. (a) Raman spectra of MoS_2 only area (black dotted line) and the stacked area (red dotted line) for MoS_2−BP heterostack. The stacked area has both the MoS_2 peaks and BP peaks. (b) Raman spectra of WS_2 only area (black dotted line) and the stacked area (red dotted line) for WS_2−BP heterostack. (c) PL spectra for the same areas as in (a). (d) PL spectra for the same areas as in (b). (e and f) Electronic band structure of the (e) MoS_2−BP and (f) WS_2−BP heterostacks. The bands projected onto W, Mo, and P atoms are distinguished by green, blue, and pink circles. Inset: schematic band alignment and illustrative transfer of photoexcited carriers within these heterobilayers.

where L and W are the channel length and width. C_i, the capacitance between the channel and the back gate per unit area, is estimated to be 1.3×10^{-4} Fm^{-2} ($C_i = \varepsilon_0\varepsilon_r/d$, where $\varepsilon_r = 3.9$ and $d = 285$ nm). We next evaluate the photocurrent properties of these devices using a 543 nm laser. The IV characteristics measured for three light intensities are shown in Figure 4c. From these measurements, we estimate the external quantum efficiency of 8% using the relationship,

$$\mathrm{EQE} = \frac{(I_{ds}/e)}{(P/E_\lambda)} \qquad (2)$$

where I_{ds} is the photocurrent, e is the electron charge, P is the light power, and E_λ is the photon energy. We also measure the gate dependent photocurrent properties of the devices showing higher response in the device at negative gate voltages. This is understandable since similar to MoS_2 devices, the contact Schottky barrier at negative bias can filter the stray current in the device, resulting in better photoresponse in the devices. We also estimate the photoresponsivity of our device at −80 V gate voltage. Our results show reasonable sensitivities comparable to previous measurements on MoS_2 and silicon photodetectors. Overall, our electrical and photocurrent results show good characteristics with great potential for the stacked structure in future opto-electrical applications. It is anticipated that tailoring stacking materials (replacing MoS_2 or WS_2

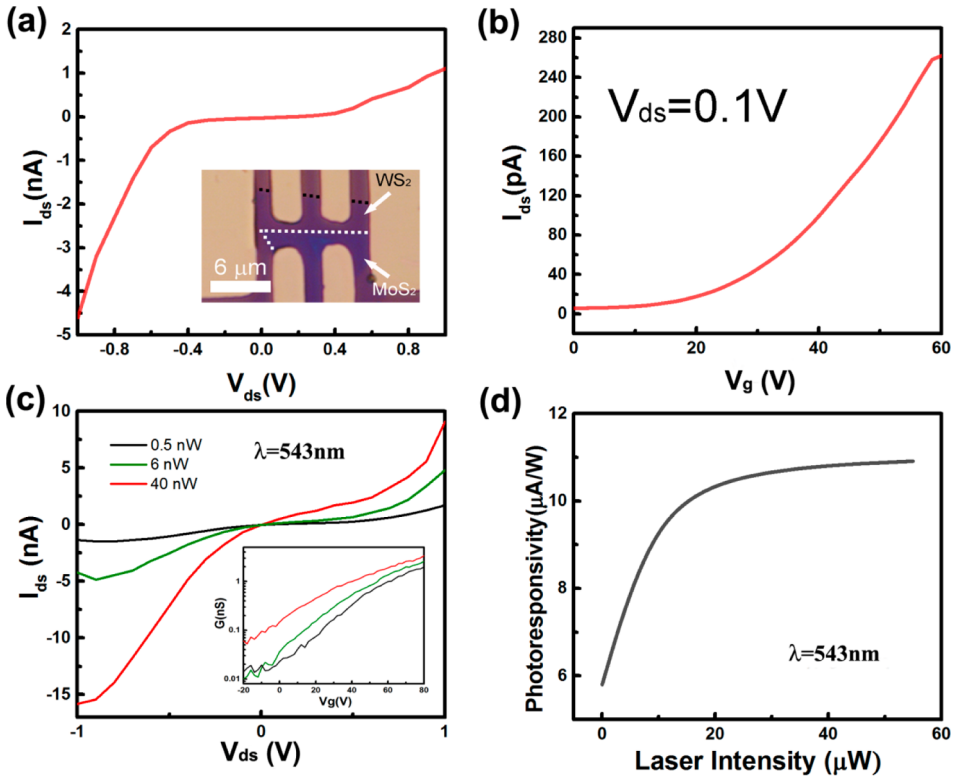

Figure 4. (a) Current−voltage (IV) curve on a representative device made on MoS_2−WS_2 heterostructures. Inset: The device geometry used in our measurements. (b) Transfer curves at V_{ds} = 0.1 V and V_g from 0 to 60 V. (c) Photocurrent properties of these devices using a 543 nm laser at different power (0.5, 6, and 40 nW). (d) Photoresponsivity of the devices at different laser intensity using a 543 nm laser.

with BP, for example) or contact electrode materials allows for better charge injection and collection providing better photodetection and photovoltaic properties in these devices. Actually, one recent work has demonstrated that p-type black phosphorus/n-type monolayer MoS_2 stack shows a maximum photodetection responsivity of 418 mA/W.[47] Further investigations on different configurations of these heterostructures are worthy to be thoroughly explored.

CONCLUSION

In this paper, we study the interlayer coupling behaviors of stacked MoS_2, WS_2 bilayers, heterobilayers of MoS_2 and WS_2 with varied stacking order and MoS_2−BP, WS_2−BP heterostacks. We demonstrate that while only WS_2 has a significant PL quenching effect in the artificially stacked heterobilayers of MoS_2 and WS_2 regardless of the stacking orders, both MoS_2 and WS_2 show dramatic quenching in MoS_2−BP and WS_2−BP heterostacks. Meanwhile, both PL peaks of MoS_2 and WS_2 have a blue-shift after forming a heterostack with few-layer BP. Our first-principles calculations indicate that the interactions between the MoS_2 and WS_2 layers retain a direct band gap at the K point for MoS_2, while forming an indirect gap for the WS_2 gives rise to the corresponding significantly weakened PL peak in WS_2. In MoS_2−BP and WS_2−BP heterostacks, the MoS_2−BP heterostack shows a type-II band alignment and WS_2−BP heterostack has a type-I band alignment. Even both of the component layers still have a direct band gap; the build-in electric fields in these heterostacks are strong enough to split the excitons, leading to a significant reduction in their recombination and subsequently a strongly quenched PL peak of the WS_2 and MoS_2. In addition, the band gap of MX_2 monolayer in these heterostructures is slightly reduced by about 10 meV as compared to the value in the freestanding case, which is in excellent agreement with our measured blue-shift of the corresponding PL peaks. Finally, our photocurrent measurements demonstrate reasonable electrical and photocurrent properties in typical MoS_2−WS_2 heterostacks, offering promising potential applications of these artificial heterostacks in future photodetector and photovoltaic devices.

METHODS

PL Measurements. PL measurements were performed by focusing the laser radiation centered at 514 nm from an argon-ion laser onto the stacks *via* a 50× objective lens. The laser excitation power was about 25 μW at the sample. The reflectance radiation was collected and analyzed using a grating spectrometer equipped with a liquid nitrogen cooled charge-coupled device camera.

Device Fabrication. Using conventional photolithography processes followed by e-beam evaporation, the field effect devices were prepared on the MoS_2—WS_2 heterostacks. For the lithography process, we used photoresist S1813 and LOR8 as an adhesive layer, and mask aligner (SUSS Mask Aligner MJB4). Ti/Au (4 nm/36 nm) were used for metallization of photolithography patterns and to fabricate the source and drain electrodes. The photoresist was removed by acetone and PG-REMOVER.

Transport Measurements. All electrical measurements are performed in a Lakeshore probe station under vacuum conditions ($<10^{-5}$ Torr) to minimize environmental effects. The device was analyzed using an Agilent B1500A Semiconductor Device Analyzer. The photocurrent measurements were performed using a 543 nm laser at different power and an applied gate voltage ranging from 0 to 60 V.

Theoretical Methods. Calculations were performed with the Vienna *Ab Initio* Simulation Package (VASP),[40,41] using the projector-augmented wave method[42] for the core region and density functional theory (DFT) based on the generalized gradient approximation (GGA) of Perdew-Burke-Emzerhof[48] with a plane-wave kinetic energy cutoff of 350 eV. A vacuum layer of 20 Å isolates neighboring periodic images and the Brillion zone is sampled by 16 *k*-points for geometry relaxation and 60 *k*-points for band structure calculations. All atomic positions are relaxed using conjugate-gradient techniques until the force on each atom is less than 0.01 eV/Å. When calculating the electronic structures, we take into account the spin—orbit coupling effect for the MX_2—BP heterostructure bilayer. For the MoS_2—BP heterobilayers, spin-unpolarized DFT is used since the spin—orbit coupling cannot be computationally afforded for the large supercell and it only qualitatively modifies the band structures.

Conflict of Interest: The authors declare no competing financial interest.

Acknowledgment. This work was supported by the Welch Foundation grant C-1716, the NSF grant ECCS- 1327093, and the U.S. Army Research Office MURI grant W911NF-11-1-0362. The authors thank W. Chen, P. Loya, E. Hacopian, M. Jiang, Y. Yang and X. Zhou for their help in experiments and discussions.

Supporting Information Available: Additional information include transfer process, characterization of bilayer MoS_2 and WS_2, and theory and calculations. This material is available free of charge *via* the Internet at http://pubs.acs.org.

REFERENCES AND NOTES

1. Novoselov, K. S.; Geim, A. K.; Morozov, S. V.; Jiang, D.; Zhang, Y.; Dubonos, S. V.; Grigorieva, I. V.; Firsov, A. A. Electric Field Effect in Atomically Thin Carbon Films. *Science* **2004**, *306*, 666–669.
2. Novoselov, K. S.; Fal'ko, V. I.; Colombo, L.; Gellert, P. R.; Schwab, M. G.; Kim, K. A Roadmap for Graphene. *Nature* **2012**, *490*, 192–200.
3. Hao, Y.; Bharathi, M. S.; Wang, L.; Liu, Y.; Chen, H.; Nie, S.; Wang, X.; Chou, H.; Tan, C.; Fallahazad, B.; *et al.* The Role of Surface Oxygen in the Growth of Large Single-Crystal Graphene on Copper. *Science* **2013**, *342*, 720–723.
4. Chen, Z. P.; Ren, W. C.; Gao, L. B.; Liu, B. L.; Pei, S. F.; Cheng, H. M. Three-Dimensional Flexible and Conductive Interconnected Graphene Networks Grown by Chemical Vapour Deposition. *Nat. Mater.* **2011**, *10*, 424–428.
5. Schwierz, F. Graphene Transistors. *Nat. Nanotechnol.* **2010**, *5*, 487–496.
6. Yuan, J.; Ma, L. P.; Pei, S.; Du, J.; Su, Y.; Ren, W.; Cheng, H. M. Tuning the Electrical and Optical Properties of Graphene by Ozone Treatment for Patterning Monolithic Transparent Electrodes. *ACS Nano* **2013**, *7*, 4233–4241.
7. Geim, A. K. Graphene: Status and Prospects. *Science* **2009**, *324*, 1530–1534.
8. Novoselov, K. S.; Jiang, D.; Schedin, F.; Booth, T. J.; Khotkevich, V. V.; Morozov, S. V.; Geim, A. K. Two-Dimensional Atomic Crystals. *Proc. Natl. Acad. Sci. U.S.A.* **2005**, *102*, 10451–10453.
9. Dean, C. R.; Young, A. F.; Meric, I.; Lee, C.; Wang, L.; Sorgenfrei, S.; Watanabe, K.; Taniguchi, T.; Kim, P.; Shepard, K. L. Boron Nitride Substrates for High-Quality Graphene Electronics. *Nat. Nanotechnol.* **2010**, *5*, 722–726.
10. Wang, Q. H.; Kalantar-Zadeh, K.; Kis, A.; Coleman, J. N.; Strano, M. S. Electronics and Optoelectronics of Two-Dimensional Transition Metal Dichalcogenides. *Nat. Nanotechnol.* **2012**, *7*, 699–712.
11. Mak, K. F.; Lee, C.; Hone, J.; Shan, J.; Heinz, T. F. Atomically Thin MoS_2: A New Direct-Gap Semiconductor. *Phys. Rev. Lett.* **2010**, *105*, 136805.
12. Liu, L.; Park, J.; Siegel, D. A.; McCarty, K. F.; Clark, K. W.; Deng, W.; Basile, L.; Idrobo, J. C.; Li, A. P.; Gu, G. Heteroepitaxial Growth of Two-Dimensional Hexagonal Boron Nitride Templated by Graphene Edges. *Science* **2014**, *343*, 163–167.
13. Liu, Z.; Ma, L.; Shi, G.; Zhou, W.; Gong, Y.; Lei, S.; Yang, X.; Zhang, J.; Yu, J.; Hackenberg, K. P.; *et al.* In-Plane Heterostructures of Graphene and Hexagonal Boron Nitride with Controlled Domain Sizes. *Nat. Nanotechnol.* **2013**, *8*, 119–124.
14. Lei, S.; Ge, L.; Najmaei, S.; George, A.; Kappera, R.; Lou, J.; Chhowalla, M.; Yamaguchi, H.; Gupta, G.; Vajtai, R.; *et al.* Evolution of the Electronic Band Structure and Efficient Photo-Detection in Atomic Layers of InSe. *ACS Nano* **2014**, *8*, 1263–1272.
15. Lei, S.; Ge, L.; Liu, Z.; Najmaei, S.; Shi, G.; You, G.; Lou, J.; Vajtai, R.; Ajayan, P. M. Synthesis and Photoresponse of Large GaSe Atomic Layers. *Nano Lett.* **2013**, *13*, 2777–2781.
16. Tongay, S.; Sahin, H.; Ko, C.; Luce, A.; Fan, W.; Liu, K.; Zhou, J.; Huang, Y. S.; Ho, C. H.; Yan, J.; *et al.* Monolayer Behaviour in Bulk ReS_2 Due to Electronic and Vibrational Decoupling. *Nat. Commun.* **2014**, *5*, 3252.
17. Coleman, J. N.; Lotya, M.; O'Neill, A.; Bergin, S. D.; King, P. J.; Khan, U.; Young, K.; Gaucher, A.; De, S.; Smith, R. J.; *et al.* Two-Dimensional Nanosheets Produced by Liquid Exfoliation of Layered Materials. *Science* **2011**, *331*, 568–571.
18. Chhowalla, M.; Shin, H. S.; Eda, G.; Li, L. J.; Loh, K. P.; Zhang, H. The Chemistry of Two-Dimensional Layered Transition Metal Dichalcogenide Nanosheets. *Nat. Chem.* **2013**, *5*, 263–275.
19. Tang, D. M.; Kvashnin, D. G.; Najmaei, S.; Bando, Y.; Kimoto, K.; Koskinen, P.; Ajayan, P. M.; Yakobson, B. I.; Sorokin, P. B.; Lou, J.; *et al.* Nanomechanical Cleavage of Molybdenum Disulphide Atomic Layers. *Nat. Commun.* **2014**, *5*, 3631.
20. Matte, H. S.; Gomathi, A.; Manna, A. K.; Late, D. J.; Datta, R.; Pati, S. K.; Rao, C. N. MoS_2 and WS_2 Analogues of Graphene. *Angew. Chem. Int. Ed.*. **2010**, *49*, 4059–4062.
21. Lee, Y. H.; Zhang, X. Q.; Zhang, W.; Chang, M. T.; Lin, C. T.; Chang, K. D.; Yu, Y. C.; Wang, J. T.; Chang, C. S.; Li, L. J.; *et al.* Synthesis of Large-Area MoS_2 Atomic Layers with Chemical Vapor Deposition. *Adv. Mater.* **2012**, *24*, 2320–2325.
22. Zhan, Y.; Liu, Z.; Najmaei, S.; Ajayan, P. M.; Lou, J. Large-Area Vapor-Phase Growth and Characterization of MoS_2Atomic Layers on a SiO_2 Substrate. *Small* **2012**, *8*, 966–971.
23. Najmaei, S.; Liu, Z.; Zhou, W.; Zou, X.; Shi, G.; Lei, S.; Yakobson, B. I.; Idrobo, J. C.; Ajayan, P. M.; Lou, J. Vapour Phase Growth and Grain Boundary Structure of Molybdenum Disulphide Atomic Layers. *Nat. Mater.* **2013**, *12*, 754–759.
24. Splendiani, A.; Sun, L.; Zhang, Y. B.; Li, T. S.; Kim, J.; Chim, C. Y.; Galli, G.; Wang, F. Emerging Photoluminescence in Monolayer MoS_2. *Nano Lett.* **2010**, *10*, 1271–1275.
25. Zhao, W.; Ribeiro, R. M.; Toh, M.; Carvalho, A.; Kloc, C.; Castro Neto, A. H.; Eda, G. Origin of Indirect Optical Transitions in Few-Layer MoS_2, WS_2, and WSe_2. *Nano Lett.* **2013**, *13*, 5627–5634.
26. Terrones, H.; Lopez-Urias, F.; Terrones, M. Novel Hetero-Layered Materials with Tunable Direct Band Gaps by Sandwiching Different Metal Disulfides and Diselenides. *Sci. Rep.* **2013**, *3*, 1549.
27. Zhu, B.; Zeng, H.; Dai, J.; Gong, Z.; Cui, X. Anomalously Robust Valley Polarization and Valley Coherence in

Bilayer WS_2. *Proc. Natl. Acad. Sci. U.S.A.* **2014**, *111*, 11606–11611.
28. Najmaei, S.; Zou, X.; Er, D.; Li, J.; Jin, Z.; Gao, W.; Zhang, Q.; Park, S.; Ge, L.; Lei, S.; *et al.* Tailoring the Physical Properties of Molybdenum Disulfide Monolayers by Control of Interfacial Chemistry. *Nano Lett.* **2014**, *14*, 1354–1361.
29. Georgiou, T.; Jalil, R.; Belle, B. D.; Britnell, L.; Gorbachev, R. V.; Morozov, S. V.; Kim, Y. J.; Gholinia, A.; Haigh, S. J.; Makarovsky, O.; *et al.* Vertical Field-Effect Transistor Based on Graphene-WS_2 Heterostructures for Flexible and Transparent Electronics. *Nat. Nanotechnol.* **2013**, *8*, 100–103.
30. Yu, W. J.; Li, Z.; Zhou, H.; Chen, Y.; Wang, Y.; Huang, Y.; Duan, X. Vertically Stacked Multi-Heterostructures of Layered Materials for Logic Transistors and Complementary Inverters. *Nat. Mater.* **2013**, *12*, 246–252.
31. Britnell, L.; Ribeiro, R. M.; Eckmann, A.; Jalil, R.; Belle, B. D.; Mishchenko, A.; Kim, Y. J.; Gorbachev, R. V.; Georgiou, T.; Morozov, S. V.; *et al.* Strong Light-Matter Interactions in Heterostructures of Atomically Thin Films. *Science* **2013**, *340*, 1311–1314.
32. Fang, H.; Battaglia, C.; Carraro, C.; Nemsak, S.; Ozdol, B.; Kang, J. S.; Bechtel, H. A.; Desai, S. B.; Kronast, F.; Unal, A. A.; *et al.* Strong Interlayer Coupling in Van der Waals Heterostructures Built from Single-Layer Chalcogenides. *Proc. Natl. Acad. Sci. U.S.A.* **2014**, *111*, 6198–6202.
33. Tongay, S.; Fan, W.; Kang, J.; Park, J.; Koldemir, U.; Suh, J.; Narang, D.; Liu, K.; Ji, J.; Li, J.; *et al.* Tuning Interlayer Coupling in Large-area Heterostructures with CVD-Grown MoS_2 and WS_2 Monolayers. *Nano Lett.* **2014**, *14*, 3185–3190.
34. van der Zande, A. M.; Kunstmann, J.; Chernikov, A.; Chenet, D. A.; You, Y.; Zhang, X.; Huang, P. Y.; Berkelbach, T. C.; Wang, L.; Zhang, F.; *et al.* Tailoring the Electronic Structure in Bilayer Molybdenum Disulfide *via* Interlayer Twist. *Nano Lett.* **2014**, *14*, 3869–3875.
35. Hong, X.; Kim, J.; Shi, S.; Zhang, Y.; Jin, C.; Sun, Y.; Tongay, S.; Wu, J.; Zhang, Y.; Wang, F. Ultrafast Charge Transfer in Atomically Thin MoS_2/WS_2 Heterostructures. *Nat. Nanotechnol.* **2014**, *9*, 682–686.
36. Li, L.; Yu, Y.; Ye, G. J.; Ge, Q.; Ou, X.; Wu, H.; Feng, D.; Chen, X. H.; Zhang, Y. Black Phosphorus Field-Effect Transistors. *Nat. Nanotechnol.* **2014**, *9*, 372–377.
37. Liu, H.; Neal, A. T.; Zhu, Z.; Luo, Z.; Xu, X.; Tomanek, D.; Ye, P. D. Phosphorene: An Unexplored 2D Semiconductor with a High Hole Mobility. *ACS Nano* **2014**, *8*, 4033–4041.
38. Komsa, H.-P.; Krasheninnikov, A. V. Effects of Confinement and Environment on the Electronic Structure and Exciton Binding Energy of MoS_2 from First Principles. *Phys. Rev. B* **2012**, *86*, 241201.
39. Bernardi, M.; Palummo, M.; Grossman, J. C. Extraordinary Sunlight Absorption and One Nanometer Thick Photovoltaics Using Two-Dimensional Monolayer Materials. *Nano Lett.* **2013**, *13*, 3664–3670.
40. Kresse, G.; Hafner, J. *Ab Initio* Molecular-Dynamics Simulation of the Liquid-Metal–Amorphous-Semiconductor Transition in Germanium. *Phys. Rev. B* **1994**, *49*, 14251–14269.
41. Kresse, G. Efficient Iterative Schemes for *ab Initio* Total-Energy Calculations Using a Plane-Wave Basis Set. *Phys. Rev. B* **1996**, *54*, 11169–11186.
42. Blöchl, P. E. Projector Augmented-Wave Method. *Phys. Rev. B* **1994**, *50*, 17953–17979.
43. Qiu, D. Y.; da Jornada, F. H.; Louie, S. G. Optical Spectrum of MoS_2: Many-Body Effects and Diversity of Exciton States. *Phys. Rev. Lett.* **2013**, *111*, 216805.
44. Mak, K. F.; He, K.; Lee, C.; Lee, G. H.; Hone, J.; Heinz, T. F.; Shan, J. Tightly Bound Trions in Monolayer MoS_2. *Nat. Mater.* **2013**, *12*, 207–211.
45. Mouri, S.; Miyauchi, Y.; Matsuda, K. Tunable Photoluminescence of Monolayer MoS_2 *via* Chemical Doping. *Nano Lett.* **2013**, *13*, 5944–5948.
46. Peimyoo, N.; Yang, W.; Shang, J.; Shen, X.; Wang, Y.; Yu, T. Chemically Driven Tunable Light Emission of Charged and Neutral Excitons in Monolayer WS_2. *ACS Nano* **2014**, *8*, 11320–11329.
47. Deng, Y.; Luo, Z.; Conrad, N. J.; Liu, H.; Gong, Y.; Najmaei, S.; Ajayan, P. M.; Lou, J.; Xu, X.; Ye, P. Black Phosphorus–Monolayer MoS_2 Van der Waals Heterojunction p–n Diode. *ACS Nano* **2014**, *8*, 8292–8299.
48. Perdew, J. P.; Burke, K.; Ernzerhof, M. Generalized Gradient Approximation Made Simple. *Phys. Rev. Lett.* **1996**, *77*, 3865–3868.